JASA ARTICLE

Mid-frequency acoustic localization of breaking waves

Ryan Saenger,[a] Luc Lenain, and William S. Hodgkiss
Scripps Institution of Oceanography, University of California San Diego, La Jolla, California 92093, USA

ABSTRACT:
During an experiment in deep water off the coast of Southern California, wind speeds ranged from 10 to 15 m/s and wind forcing produced large breaking waves. A mid-frequency vertical planar hydrophone array recorded underwater ambient noise while an airplane equipped with a high-resolution video camera captured images of the sea surface above the array. Beams of ambient noise between 5 and 6 kHz were projected onto the sea surface and synchronized in space and time with the aerial images. Despite the array's limited azimuthal resolution of the surface, due to its modest 1 m horizontal aperture and relatively deep 130 m deployment depth, concentrated areas of high intensity in the acoustic surface projection were observed to match visible breaking events in the aerial images.
 https://doi.org/10.1121/10.0021969

(Received 24 May 2023; revised 3 October 2023; accepted 5 October 2023; published online 24 October 2023)

[Editor: Karim G. Sabra] Pages: 2564–2571

I. INTRODUCTION

Breaking waves are the dominant natural source of surface-generated ocean noise. Laboratory experiments[1–5] suggest that the principal mechanism by which breaking waves generate sound at frequencies greater than 500 Hz is the entrainment of bubbles that briefly oscillate on creation. The mid-frequency (1–10 kHz) acoustic signature of a surface wave is, therefore, confined to the time during which the wave is actively breaking. Individual breaking events have been observed acoustically as transient peaks in mid-frequency power spectral density (PSD) on shallow hydrophones from the surf zone[6,7] to the continental shelf[8] and deep ocean.[9] The area of ocean surface that contributes substantially to ambient noise PSD increases with hydrophone depth. Consequently, the temporal variance of PSD on time scales of seconds decreases with hydrophone depth because a deep hydrophone integrates over a larger radius on the surface than a shallow one. Single-hydrophone measurements of individual breaking events are generally restricted to shallow deployments.

Hydrophone arrays need not be as close to the surface as single hydrophones to detect wave breaking events because they can separate acoustic sources in space. Field experiments have demonstrated localization and even tracking of breaking wave trajectories. Ding and Farmer[9–11] tracked breaking waves along the ocean surface by calculating time-domain cross correlations of horizontally separated hydrophones suspended 25 m below the surface.

Most analogous to the results presented here is the extensive study of surface-generated high-frequency (10–50 kHz) noise undertaken by Crowther and Hansla[12] in 80 m water with a bottom-mounted, upward-looking array. They found that tracks of spatially concentrated ambient noise followed the trajectories of breaking waves visible on recorded video and acoustic power coincided in time with active breaking.

In this experiment, breaking waves were localized acoustically with a mid-frequency noise array (MFNA) deployed 130 m below the surface, and acoustic events were matched to synchronized aerial images of the ocean surface above the array (Fig. 1). The relatively deep deployment of the MFNA, compared to those of instruments used in past studies of surface noise, was due to the fact that the TFOEx21 experiment was primarily intended to study acoustic propagation at elevation angles close to horizontal ($\theta = 0$). The deep location of the MFNA limited its resolution of surface sources but enabled observation of a larger area of ocean surface than that observed in preceding field measurements. The listening radius at 130 m depth, as defined by Farmer and Vagle,[8] is about 180 m at 6 kHz. Breaking events were observed throughout a 250 m observation radius on the surface.

II. ENVIRONMENT

The TFOEx21 experiment took place 500 km west of San Diego in 4000 m deep water. The part of the experiment described here is a segment of one flight during which the MFNA was in the field of view of the Modular Aerial Sensing System (MASS). This flyover occurred on 2021–05-09 from 21:05:59 to 21:07:41 UTC (14:05:59–14:07:41 local time), during which time the MFNA recorded ambient noise. All times reported here are UTC unless otherwise specified.

Directional surface wave spectra were measured by an instrumented Wave Glider (Boeing Liquid Robotics SV3, Herndon, VA); detailed description of available instrumentation and processing is presented in Grare *et al.*[13] The significant wave height (H_s) during the flyover was 4 m [Fig. 2(b)]. The dominant wave period was about 10 s

[a]Email: rsaenger@ucsd.edu

https://doi.org/10.1121/10.0021969

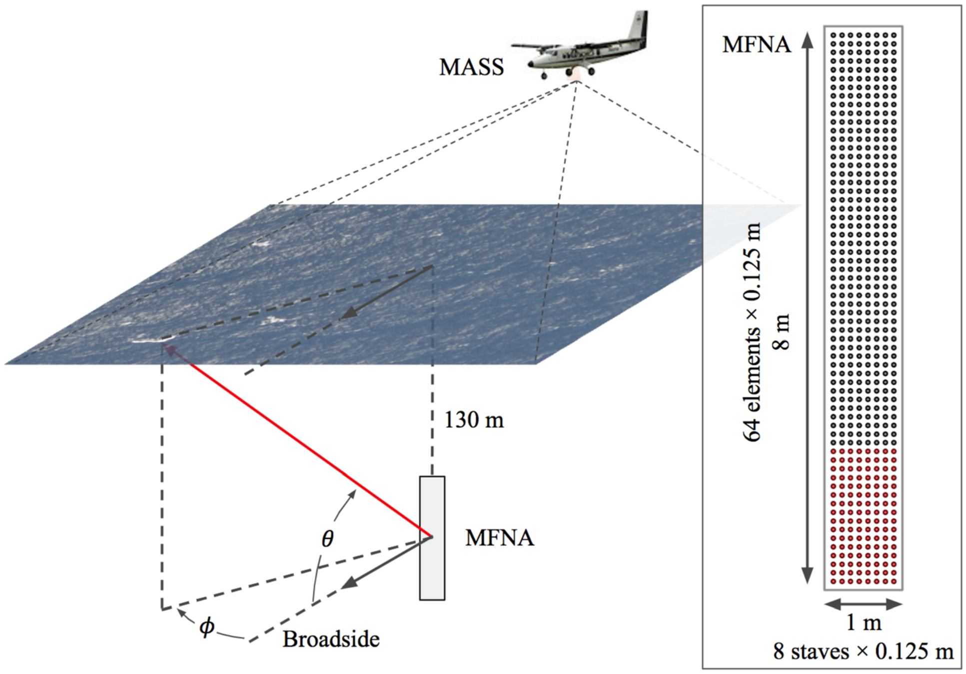

FIG. 1. (Color online) Experiment schematic. Surface images and ambient noise were simultaneously recorded with the MASS and the MFNA, respectively. The MFNA consists of 8 vertical staves of 64 elements each. Only the top 48 elements from each stave (pictured in black) were included in the results shown here. Elevation (θ) and azimuth (ϕ) are defined with respect to broadside.

[Fig. 2(c)]. The Wave Glider also carried two ultrasonic anemometers that measured wind speed and direction. Winds greater than 10 m/s were sustained for approximately 60 h before the flyover [Fig. 2(a)], so the sea was well developed.

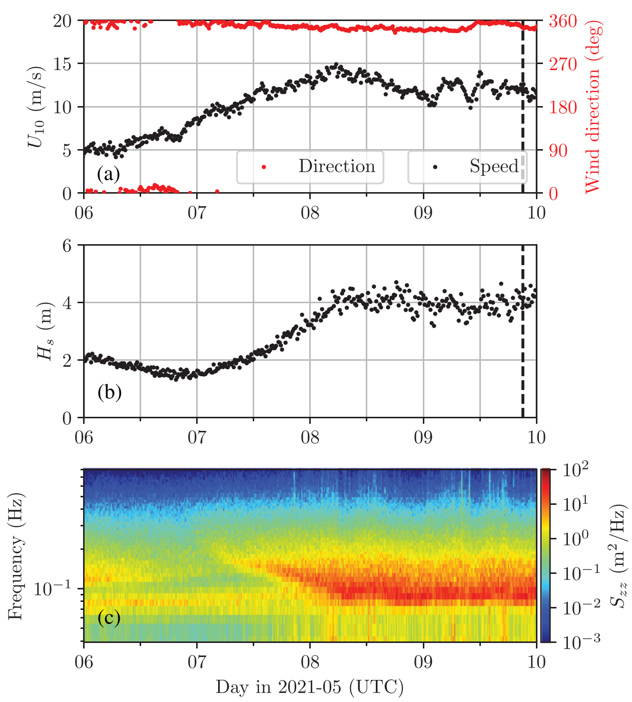

FIG. 2. (Color online) Wind and waves over four days leading up to the flight. During the flight on 2021-5-9 from 21:05:59 to 21:06:41 (vertical dashed line), the wind was 11 m/s from north-northwest. The significant wave height was 4 m. The dominant wave period was about 10 s and incident from north-northwest.

The wind and wave directions were nearly aligned at a heading of about 340 deg.

The sound speed profile (SSP) was calculated by Del Grosso's method[14] from 60 min (2021-5-9 20:30–21:30 UTC) of temperature measurements made by a thermistor chain and a Wirewalker (Del Mar Oceanographic, San Diego, CA). The thermistor chain and Wirewalker were linked together and located 3 km from the MFNA at the time of the flyover. From 0 to 50 m deep, 17 thermistors with 2.9 m spacing measured temperature. The Wirewalker measured both temperature and salinity between 50 and 100 m. From 100 to 200 m, 34 more thermistors with 2.9 m spacing measured temperature. A complete salinity profile was obtained by combining the Wirewalker salinity measurement with salinity from a later conductivity–temperature–depth (CTD) cast on 2021-5-11 at 16:14 UTC. The Wirewalker measurements were combined with thermistor chain measurements to make a complete SSP from 0 to 200 m.

The mean SSP was downward refracting below the mixed layer, which was about 40 m deep. Rays were traced from the MFNA to the surface with Bellhop.[15] Within the 250 m observation radius at the surface, measured from the point on the surface directly above the MFNA, refraction is weak because the propagation ranges are short and the angles are steep. Rays through the measured SSP are similar to those through an isospeed medium. For a given launch angle from the MFNA, the range at which a ray through an isospeed medium intersects the surface is within 7.5 m of the range at which a ray through the measured SSP intersects the surface. This is a modest discrepancy relative to the radial beam width at a range of 250 m, which is nearly

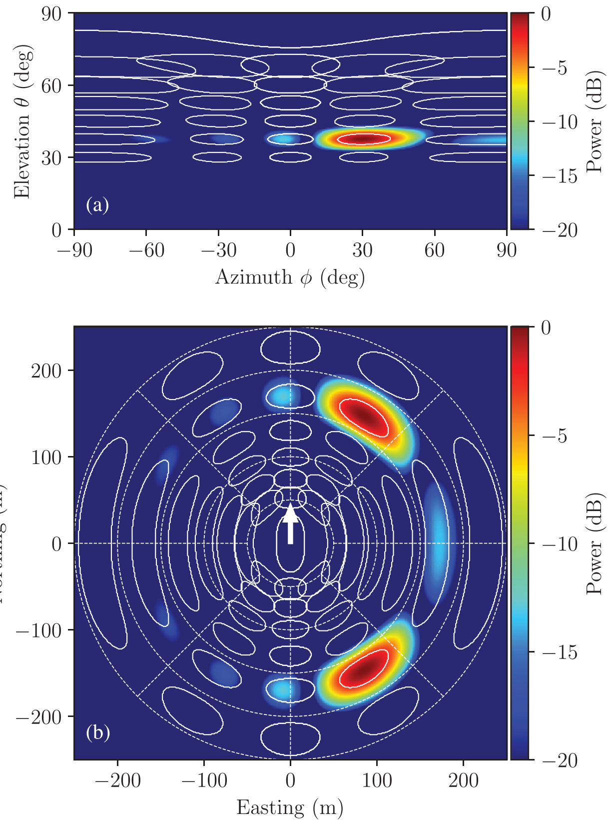

FIG. 3. (Color online) (a) Conventional beam pattern of a simulated 5 kHz plane wave incident from 37.5° elevation and 30° azimuth on the 48×8 element MFNA and (b) its projection onto the surface. Overlaid on beam pattern are 3-dB beam contours for 5 kHz plane waves incident from 30° to 67.5° in elevation in 7.5° increments and 0°, ±30°, and ±90° in azimuth, as well as 90° elevation (overhead). A spatial Kaiser window ($\beta = 1.5\pi$) is applied to the vertical aperture and a rectangular window is applied to the horizontal aperture. One mainlobe in elevation and azimuth becomes two in northing and easting due to the front-back ambiguity of the MFNA. The weights are not adaptive for this demonstrative example. Broadside points north.

50 m [Fig. 3(b)], but the assumption of an isospeed profile makes surface sources appear slightly closer in range.

III. INSTRUMENT PROPERTIES

A. MFNA

The MFNA consists of eight vertical staves separated horizontally by 0.125 m. Each stave has 64 elements that are separated vertically by 0.125 m. The MFNA was deployed at a depth of 130 m and attached to a drifting surface buoy tracked by the Global Positioning System (GPS). Intermediate floats along the cable between the surface buoy and the MFNA mechanically decoupled the MFNA from wave action on the surface. A buoyant float at the top and ballast at the bottom held the MFNA upright, but it was free to rotate in azimuth. Pitch, roll, and heading sensors recorded its orientation, and pressure sensors recorded its depth. An analog filter with a passband between 500 and 9500 Hz followed each hydrophone, and the filtered signals were sampled at $f_s = 25$ kHz. During the flyover discussed here, only the top 48 elements of each 64-element stave were recording.

B. MASS

The component of MASS used here is an imaging sensor called DoppVis,[16] which records images of the ocean surface at 2 frames/s and approximately 0.5 m resolution over wide areas. The surface footprint of the camera's field of view during the flyover was approximately 3×5 km. The images were projected onto a georeferenced grid using the aircraft's location and attitude. The MFNA was in the field of view for about 100 s during the flyover, which was enough time to capture several large wave breaking events. A 500 m box surrounding the MFNA was isolated for comparison with the acoustic measurements. The measured GPS location of the MFNA was validated in the DoppVis images.

IV. BEAMFORMING AND SURFACE PROJECTION

A. Conventional beamforming in vertical wavenumber

Frequency-domain snapshots of the recording are obtained by fast Fourier transform (FFT) of segments of length $M = 4096$ samples with a Kaiser window applied ($\beta = \alpha\pi = 2.5\pi$, where α is the parameter in the Kaiser window definition as written by Harris[17]). Each snapshot is a vector of temporal Fourier transform coefficients, one for each array element, at a specific frequency bin. The delay between snapshots is $R = 1024$ (snapshots overlap by 75%). Given time-domain pressure samples, $p_{l,m}(n)$, on element m of stave l, the rth snapshot, $\tilde{p}_{l,m}(\omega, r)$, at normalized frequency, ω, is

$$\tilde{p}_{l,m}(\omega, r) = \sum_{n=rR}^{rR+M-1} w(n - rR) p_{l,m}(n) e^{-i\omega(n-rR)}, \quad (1)$$

where snapshot number, r, begins at zero and $w(n - rR)$ is the temporal window.

Conventional beamforming in vertical wavenumber is performed on each stave independently with a spatial Kaiser window ($\beta = 1.5\pi$) applied. The normalized vertical wavenumber, k_z, is related to elevation, θ, according to

$$k_z = k d_z \sin\theta, \quad (2)$$

where $k = \omega/c$ is the wavenumber magnitude, c is the local sound speed, and d_z is the vertical spacing of array elements. Similarly, the normalized horizontal wavenumber, k_y, is

$$k_y = k d_y \cos\theta \sin\phi, \quad (3)$$

where ϕ is the azimuthal angle. Positive elevation angles correspond to downward-propagating waves. Each stave consists of $N_{\mathrm{elm}} = 48$ elements numbered in order of increasing depth, z, such that element "0" is nearest to the ocean surface and element $N_{\mathrm{elm}} - 1$ is deepest. The complex vertical beam, $x_l(\omega, k_z, r)$, on stave l at normalized vertical wavenumber k_z may be written as a discrete Fourier transform (DFT) in $-k_z$,

$$x_l(\omega, k_z, r) = \sum_{m=0}^{N_{\mathrm{elm}}-1} w_z(m)\tilde{p}_{l,m}(\omega, r)\mathrm{e}^{ik_z m}, \tag{4}$$

where $w_z(m)$ is the spatial window. To efficiently interpolate between DFT wavenumber bins, this step is implemented by FFT with zero padding. For each normalized vertical wavenumber k_z, the complex vertical beam coefficients, $x_l(\omega, k_z, r)$, from all eight staves are combined in an eight-element vector, $\mathbf{x}(\omega, k_z, r)$.

B. Sample covariance at each vertical wavenumber

Beamforming in horizontal wavenumber is then performed at each vertical wavenumber. Array covariance matrices for beamforming in horizontal wavenumber are estimated by the sample mean of $M' = 16$ outer products of $\mathbf{x}(\omega, k_z, r)$. The covariance matrix estimates overlap by $R' = 8$ snapshots. The time between covariance estimates is $R'R/f_s = 0.32$ s, and the duration of each covariance estimate is 0.65 s. The r'th covariance estimate is

$$\hat{\mathbf{R}}(\omega, k_z, r') = \frac{1}{M'} \sum_{r=r'R'}^{r'R'+M'-1} \mathbf{x}(\omega, k_z, r)\mathbf{x}^H(\omega, k_z, r). \tag{5}$$

C. Adaptive beamforming in horizontal wavenumber

For each eight-element array vector corresponding to a vertical beam from each of the eight staves, horizontal beams are formed such that output power is

$$P(\omega, k_z, k_y, r') = \mathbf{w}^H(\omega, k_z, k_y, r')\hat{\mathbf{R}}(\omega, k_z, r') \times \mathbf{w}(\omega, k_z, k_y, r'), \tag{6}$$

where the weights, $\mathbf{w}(\omega, k_z, k_y, r')$, are determined by adaptive methods to sharpen the azimuthal beam response to concentrated sources like breaking waves and suppress loud interference from the surface buoy caused by wave action. The weights are computed from a regularized version of the minimum variance distortionles response (MVDR)[18] in which a white noise constraint (WNC)[19] is imposed on the white noise gain (WNG) of the beamformer. The adaptive weights are

$$\mathbf{w}_{\mathrm{WNC}} = \frac{(\hat{\mathbf{R}} + \epsilon\mathbf{I})^{-1}\mathbf{s}}{\mathbf{s}^H(\hat{\mathbf{R}} + \epsilon\mathbf{I})^{-1}\mathbf{s}}, \tag{7}$$

subject to the constraint on WNG,

$$\frac{|\mathbf{w}_{\mathrm{WNC}}^H\mathbf{s}|^2}{\mathbf{w}_{\mathrm{WNC}}^H\mathbf{w}_{\mathrm{WNC}}} = GN, \tag{8}$$

where the N-element replica vector, $\mathbf{s}$, is normalized such that $\mathbf{s}^H\mathbf{s} = N$, and N is the number of sensors in the array. WNG is defined as the factor by which the signal to noise ratio increases due to beamforming when the noise is white. The WNG of the adaptive beamformer is GN, where G is an adjustable parameter. The WNG of a conventional beamformer with a rectangular window (uniform shading) is N; this is equivalent to choosing $G = 1$, in which case the weight vector is equal to the replica: $\mathbf{w}_{\mathrm{WNC}} = \mathbf{s}$. The diagonal loading parameter, ϵ, is chosen such that the WNC is satisfied based on the selected value of G. The adaptive weights give up some gain over white noise to suppress interferers.

For adaptive beamforming in azimuth on the MFNA, $\mathbf{s}$ is the eight-element replica of a plane wave incident on the MFNA as a function of frequency and vertical and horizontal wavenumbers. The gain factor, G, is chosen such that $10\log_{10}G = -1$ dB because this is sufficient to achieve modest focusing on concentrated sources. A lower value of G would result in an adaptive beamformer that is less robust to mismatch between the replica and the true signal.

The beams presented here are normalized so that broadband noise with unity PSD at frequency ω, incident from one direction (θ, ϕ), results in a beamformer output of unity when steered to that direction. At each frequency ω, the direction (θ, ϕ) corresponds to vertical and horizontal wavenumbers k_z and k_y as defined in Eqs. (2) and (3). In terms of beamformer output power defined by Eq. (6), the PSD in the beam is

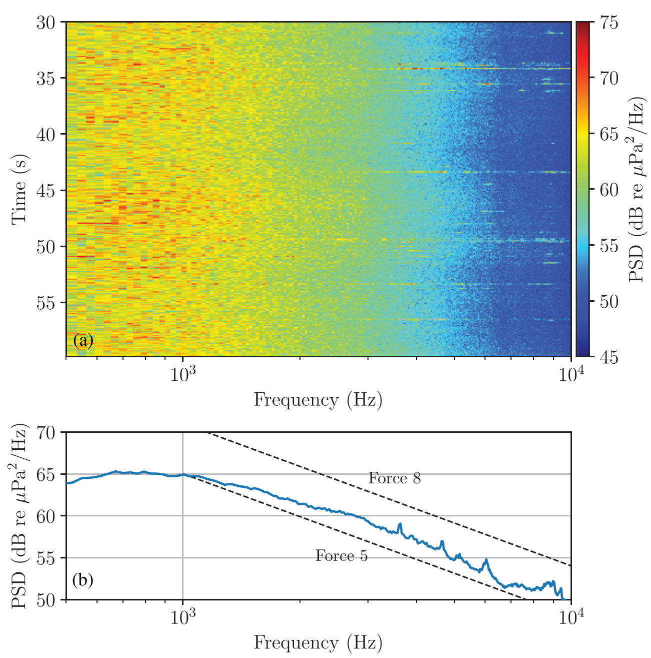

FIG. 4. (Color online) (a) Single-hydrophone ambient noise spectrogram was computed from the mean spectrogram of the 48 elements of one stave from 21:06:30 to 21:07:00, and (b) the temporal average of PSD was computed from 0.5 to 10 kHz over those 30 s. Loud transients resulting from the surface buoy are evident as thin horizontal stripes in the spectrogram and spikes between 3 and 7 kHz in the average PSD. Expected ambient noise levels (Ref. 21) at Beaufort Force 5 and Force 8 are labeled for reference. Wind speed during the flight was about 11 m/s, which is between Force 5 (8–11 m/s) and Force 6 (11–14 m/s).

$$\mathrm{PSD}(\omega, k_z, k_y) = 10\log_{10}\left[\frac{2P(\omega, k_z, k_y)}{f_s W_z^2(0) W_y^2(0)\sum_{m=0}^{M-1} w^2(m)}\right], \tag{9}$$

where $w(m)$ is the temporal window, and $W_z(0)$ and $W_y(0)$ are the first bins of the DFTs of the vertical and horizontal spatial windows, respectively. That is, $W_z(0) = 26.4$ is the sum of the samples of the 48-element vertical Kaiser window ($\beta = 1.5\pi$). Similarly, the horizontal window is an eight-element sequence of ones, therefore, $W_y(0) = 8$.

D. Surface projection of broadband beamformer output

Two-dimensional narrowband beamforming is performed at 31 frequencies spaced uniformly between 5 and 6 kHz. The mean PSD over all 31 frequencies is then geometrically projected onto the sea surface to make a map of surface-generated ambient noise. Beams in elevation and azimuth are mapped to the sea surface assuming an isovelocity SSP. This is a reasonable approximation because beam displacement due to refraction in the measured SSP is approximately 7.5 m at 250 m range from the array, which is substantially smaller than a typical beam width in range. Attenuation due to geometric spreading and source directivity is not included here; the mapping is purely geometric. Figure 3 depicts the conventional beam response of the MFNA to a plane wave incident at 37.5° elevation and 30° azimuth and its corresponding surface projection, as well as the surface projections of 3-dB beam contours for a range of directions in elevation and azimuth that map to the 250 m observation radius at the surface.

V. RESULTS

A 30 s ambient noise spectrogram for each hydrophone of stave 1 was estimated from 4096-point DFTs with a Kaiser window ($\beta = 2.5\pi$). The incoherent average of the 48 single-element spectrograms is shown in Fig. 4(a) and the 30 s average of the spectrogram is depicted in Fig. 4(b). Ambient noise levels were generally consistent with previous studies of the relationship between wind speed and noise

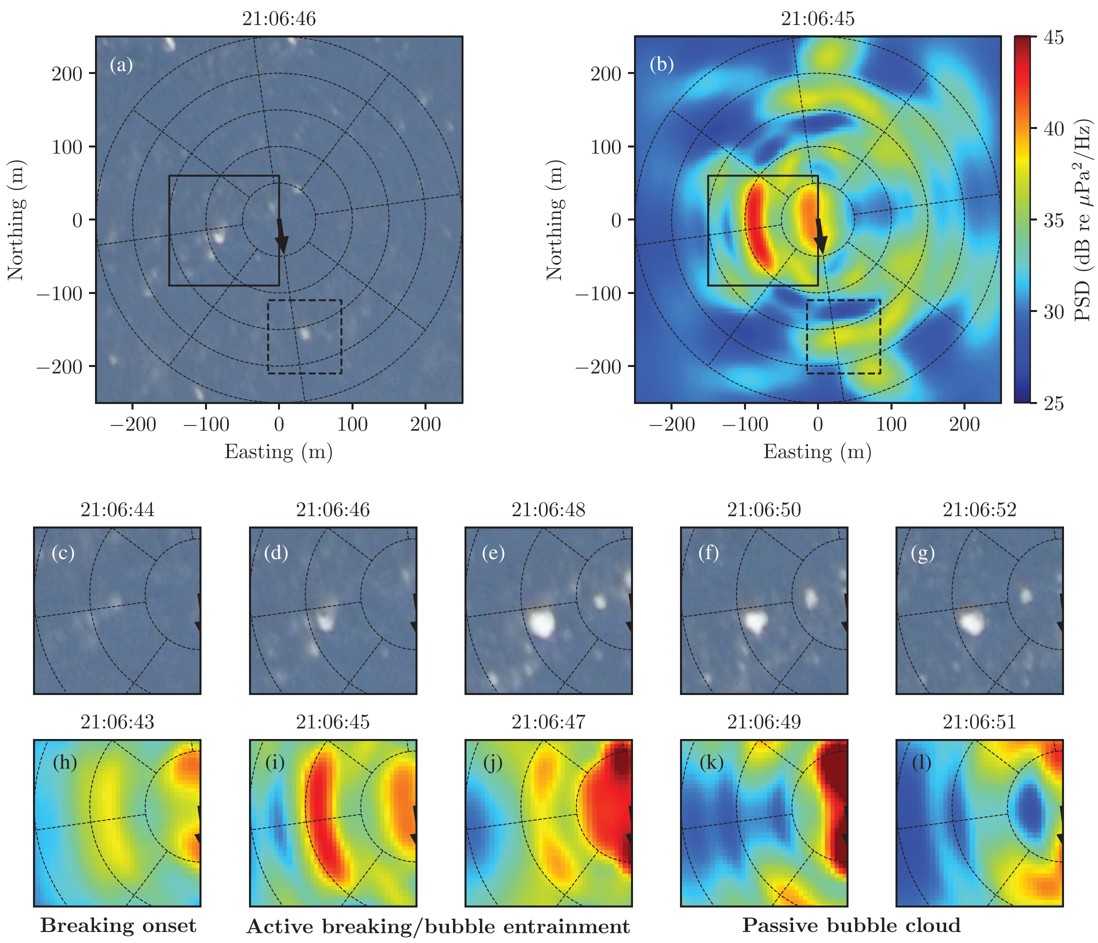

FIG. 5. (Color online) (a) Aerial image of 500 m box around MFNA during a wave breaking event near edgefire just after breaking at 21:06:45 and (b) acoustic surface projection during breaking is depicted. Broadside (black arrow) points south-southeast. The event in focus occurs at the center of the 150 m solid black box. (c)–(g) Sequence of close-up views, separated by 2 s, of aerial images and (h)–(l) surface projections in the solid black box are displayed. The high-intensity peak directly above the array [(j), (k)] is noise due to surface buoy motion. Not all white patches in (a) are actively breaking waves; many are residual foam patches from recent wave breaking events. However, there is one additional active event in view at the center of the dashed box.

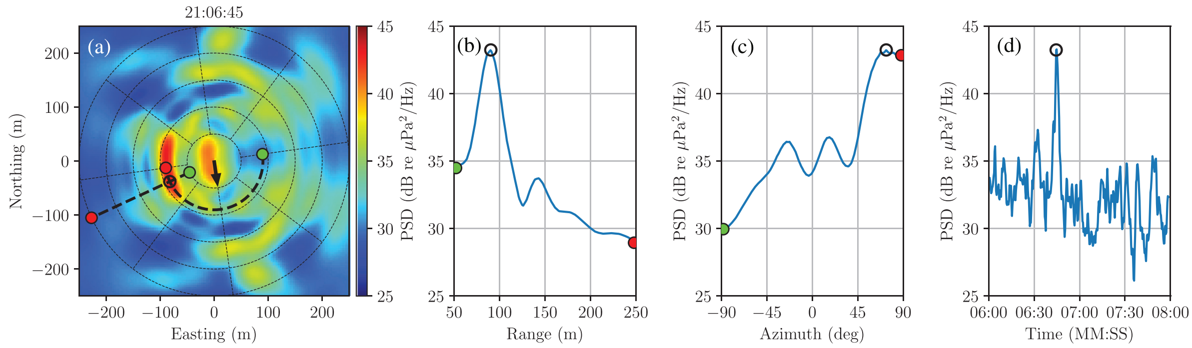

FIG. 6. (Color online) (a) Aerial image of 500 m box around MFNA during a wave breaking event near broadside at 21:06:55 and (b) acoustic surface projection just before that time are shown. Broadside (black arrow) points south-southeast. The event in focus occurs at the center of the 150 m solid black box. (c)–(g) Sequence of close-up views, separated by 2 s, of aerial images and (h)–(l) surface projections in the solid black box are displayed. Not all white patches in (a) are actively breaking waves; many are residual foam patches from recent wave breaking events. However, there is one additional active event in view at the center of the dashed box.

PSD. The slope of the ambient noise spectrum from 1 to 10 kHz was about -19 dB/decade, which is similar to that reported in past laboratory and field experiments.[3,20]

Loud, impulsive interference from the surface buoy was visible as thin horizontal stripes in the single-hydrophone spectrogram [Fig. 4(a)]. This interference was attributed to the surface buoy because it was incident from directly above the array and contained some narrowband components between 3 and 7 kHz, which were visible as spikes in the average PSD [Fig. 4(b)].

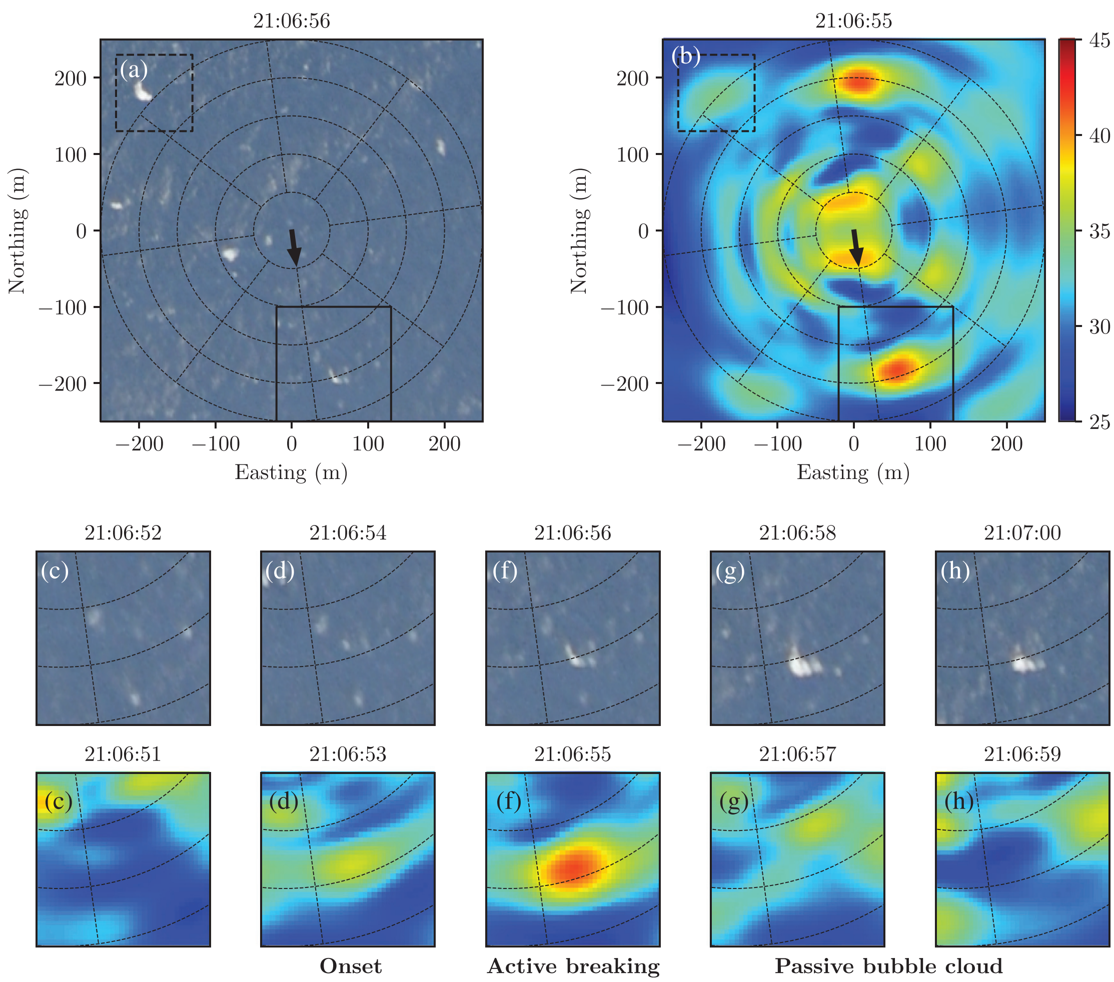

FIG. 7. (Color online) (a) Acoustic surface projection and (b) cross sections in range, (c) azimuth, and (d) time of a wave breaking event at 21:06:45 are shown. Range and azimuth cross sections follow the cut lines from green to red on the surface projection in (a). The time series in (d) represents average PSD from 5 to 6 kHz at the event location over a 2-min period. In each panel, the peak corresponding to the breaking wave is marked with an open circle.

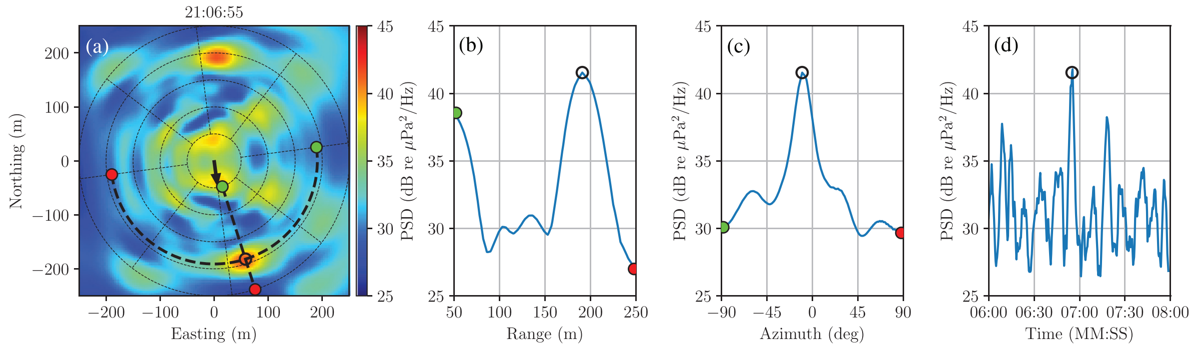

FIG. 8. (Color online) (a) Acoustic surface projection and (b) cross sections in range, (c) azimuth, and (d) time of a wave breaking event at 21:06:55 are shown. Range and azimuth cross sections follow the cut lines from green to red on the surface projection in (a). The time series in (d) represents average PSD from 5 to 6 kHz at the event location over a 2-min period. In each panel, the peak corresponding to the breaking wave is marked with an open circle.

Individual breaking waves were not evident in the single-hydrophone spectrogram, which is not surprising given the depth of the MFNA and the large region of ocean surface over which it integrates sound. However, through beamforming, several large events were clear in the acoustic surface projection and matched synchronized aerial images. Two events are depicted in Figs. 5 and 6 as sequences of images and acoustic surface projections. The first event (2021-5-9 21:06:45 UTC) occurred near edgefire in azimuth, the second (2021-5-9 21:06:55 UTC) occurred near broadside. The peak PSD of these events was about 42 dB re μPa in the surface projections, and the average single-hydrophone ambient noise level between 5 and 6 kHz was about 54 dB re μPa [Fig. 4(b)]. That the peak beamformer output level of each breaking event is less than the average ambient noise level is consistent with the fact that individual breaking waves were not distinguishable in the single-hydrophone average spectrogram. This is related to the fact that the beamformer is normalized such that a broadband source emitting plane waves from one angle of incidence results in a beamformer output equal to the PSD of the source, as discussed in Sec. IV C. Beamforming makes it possible to detect breaking events with received levels less than the average ambient noise level by focusing on sound incident from one area of the surface and suppressing all other sources.

In each case, broadside pointed nearly south and the surface projection was symmetrical in that direction because of the front-back ambiguity of the MFNA. A concentrated acoustic source appeared in the surface projection just before foam became visible in the aerial image. Elevated source level in the surface projection was coincident with the period during which the foam patch formed in the image. The foam patch persisted for tens of seconds but was

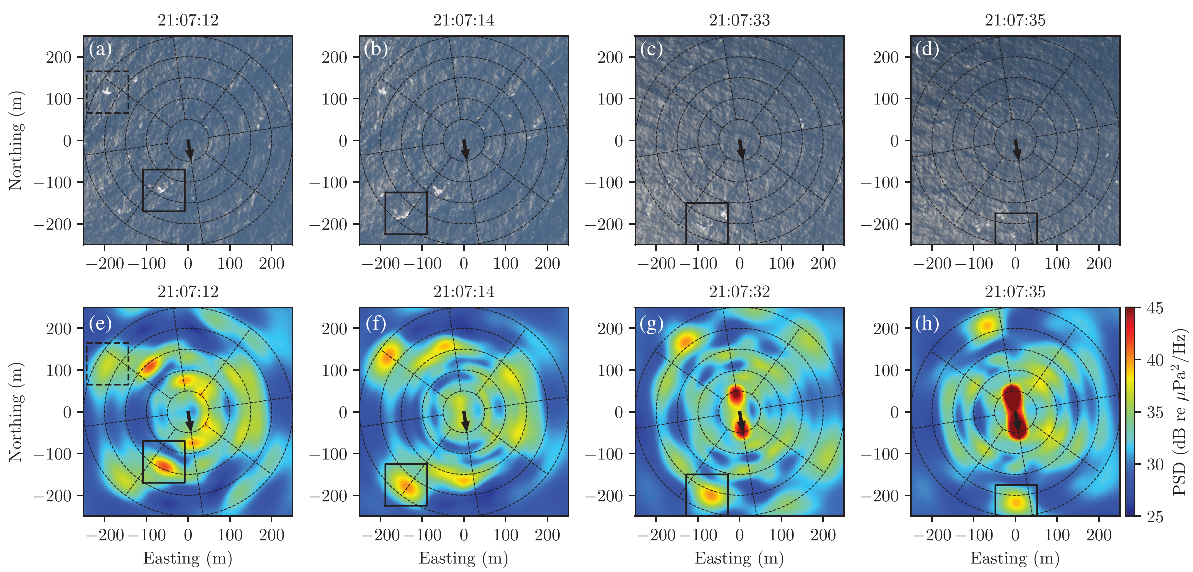

FIG. 9. (Color online) (a)–(d) Selected wave breaking event images and (e), (f) their corresponding acoustic surface projections, presented during the active breaking phase, are shown. The breaking events in focus are centered in the solid black boxes. The large foam patch in the dashed black box in (a) is an additional active breaking event with an acoustic signature in (e). Video shows that the active breaking event in the dashed box in (a) ended before 21:07:14, therefore, it did not contribute to the acoustic signature in the solid box in (f), which is due primarily to the active breaking event in the solid box in (b). The event in the solid box in (e) is still active in (f), indicating that the active breaking phase extends through frames (a) and (b), which is consistent with video. In contrast, the event in (g) vanishes before (h), indicating active breaking ended even though the foam patch from (c) is still visible in (d). This is also consistent with video.

acoustically inactive after the active phase of breaking ended. Cross sections of the acoustic surface projection in range, azimuth, and time (Figs. 7 and 8) show that these two large wave breaking events were 5–10 dB above background noise and concentrated in space and time.

Wave breaking is often difficult to see in still images because even loud breaking events do not always create foam patches as large as those in Figs. 5 and 6, and sunlight reflected from the ocean surface can be difficult to distinguish from foam. Breaking is easier to identify in video because it provides time-domain context. Reflective facets on the sea surface tend to translate continuously in the direction of wave propagation, but foam created by wave breaking appears abruptly and does not follow the wave crest after formation. The detection of active breaking events in sequences of images is well studied,[22–25] but the scope of this paper is limited to events that are clearly visible by eye in video and in the acoustic surface projection. Figure 9 shows four acoustically detectable events: two that are easily visible in still images [Figs. 9(a) and 9(b)] and two that are visible in still images but better identified in video because their foam patches are small [Figs. 9(c) and 9(d)].

VI. CONCLUSION

Direct comparison of aerial images to the acoustic surface projection provided conclusive evidence that the concentrated sources of mid-frequency ambient noise observed were the result of large breaking waves.[26] Although the array used in this experiment was limited by front-back ambiguity and relatively small horizontal aperture, its deep deployment and high array gain enabled detection of individual breaking events throughout a relatively large 250 m radius on the surface.

ACKNOWLEDGMENTS

We thank Dave Ensberg for assisting with the acoustic and heading sensor data and Jake DeFilippis for providing the thermistor chain and Wirewalker data. We also thank both reviewers for thoughtful suggestions that improved this paper. This work was supported by the Office of Naval Research under Grant No. N00014–19-1–2635.

[1]M. L. Banner and D. H. Cato, "Physical mechanisms of noise generation of breaking waves—A laboratory study," in *Sea Surface Sound: Natural Mechanisms of Surface Generated Noise in the Ocean*, NATO ASI Series C: Mathematical and Physical Sciences Vol. 238, edited by B. R. Kerman (Kluwer Academic, Boston, 1988), pp. 429–436.
[2]B. R. Kerman, "Audio signature of a laboratory breaking wave," in *Sea Surface Sound: Natural Mechanisms of Surface Generated Noise in the Ocean*, NATO ASI Series C: Mathematical and Physical Sciences Vol. 238, edited by B. R. Kerman (Kluwer Academic, Boston, 1988), pp. 437–448.
[3]H. Medwin and M. M. Beaky, "Bubble sources of the Knudsen sea noise spectra," J. Acoust. Soc. Am. **86**, 1124–1130 (1989).
[4]H. C. Pumphrey and J. E. Ffowcs Williams, "Bubbles as sources of ambient noise," IEEE J. Ocean. Eng. **15**, 268–274 (1990).
[5]M. R. Loewen and W. K. Melville, "A model of the sound generated by breaking waves," J. Acoust. Soc. Am. **90**, 2075–2080 (1991).
[6]G. B. Deane, "Sound generation and air entrainment by breaking waves in the surf zone," J. Acoust. Soc. Am. **102**, 2671–2689 (1997).
[7]G. B. Deane, "Acoustic hot-spots and breaking wave noise in the surf zone," J. Acoust. Soc. Am. **105**, 3151–3167 (1999).
[8]D. M. Farmer and S. Vagle, "On the determination of breaking surface wave distributions using ambient sound," J. Geophys. Res. **93**, 3591–3600, https://doi.org/10.1029/JC093iC04p03591 (1988).
[9]D. M. Farmer and L. Ding, "Coherent acoustical radiation from breaking waves," J. Acoust. Soc. Am. **92**, 397–402 (1992).
[10]L. Ding and D. Farmer, "A signal-processing scheme for passive acoustical mapping of breaking surface waves," J. Atmos. Ocean. Tech. **9**, 484–494 (1992).
[11]L. Ding and D. M. Farmer, "Observations of breaking surface wave statistics," J. Phys. Ocean. **24**, 1368–1387 (1994).
[12]P. A. Crowther and A. Hansla, "The lifetimes, velocities and probable origin of sonic and ultrasonic noise sources on the sea surface," in *Natural Physical Sources of Underwater Sound*, edited by B. R. Kerman (Kluwer Academic, Dordrecht, the Netherlands, 1993), pp. 379–392.
[13]L. Grare, N. A. Statom, N. Pizzo, and L. Lenain, "Instrumented wave gliders for air-sea interaction and upper-ocean research," Front. Mar. Sci. **8**, 664728 (2021).
[14]V. A. D. Grosso, "New equation for the speed of sound in natural waters (with comparisons to other equations)," J. Acoust. Soc. Am. **56**, 1084–1091 (1974).
[15]M. B. Porter, "Bellhop," available at http://oalib.hlsresearch.com (Last viewed May 19, 2023).
[16]L. Lenain, B. K. Smeltzer, N. Pizzo, M. Freilich, L. Colosi, S. Å. Ellingsen, L. Grare, H. Peyriere, and N. Statom, "Airborne remote sensing of upper-ocean and surface properties, currents and their gradients from meso to submesoscales," Geophys. Res. Let. **50**, e2022GL102468, https://doi.org/10.1029/2022GL102468 (2023).
[17]F. J. Harris, "On the use of windows for harmonic analysis with the discrete Fourier transform," Proc. IEEE **66**, 51–83 (1978).
[18]J. Capon, "High-resolution frequency-wavenumber spectrum analysis," Proc. IEEE **57**, 1408–1418 (1969).
[19]H. Cox, R. M. Zeskind, and M. M. Owen, "Robust adaptive beamforming," IEEE Trans. Acoust. Speech Signal Process. **35**, 1365–1376 (1987).
[20]S. Vagle, W. G. Large, and D. M. Farmer, "An evaluation of the WOTAN technique of inferring oceanic winds from underwater ambient sound," J. Atmos. Ocean. Tech. **7**, 576–595 (1990).
[21]G. M. Wenz, "Acoustic ambient noise in the ocean: Spectra and sources," J. Acoust. Soc. Am. **34**, 1936–1956 (1962).
[22]J. M. Kleiss and W. K. Melville, "Observations of wave breaking kinematics in fetch-limited seas," J. Phys. Ocean. **40**, 2575–2604 (2010).
[23]J. M. Kleiss and W. K. Melville, "The analysis of sea surface imagery for whitecap kinematics," J. Atmos. Ocean. Tech. **28**, 219–243 (2011).
[24]P. Sutherland and W. K. Melville, "Field measurements and scaling of ocean surface wave-breaking statistics," Geophys. Res. Let. **40**, 3074–3079, https://doi.org/10.1002/grl.50584 (2013).
[25]T. Vrećica, N. Pizzo, and L. Lenain, "Observations of strongly modulated surface wave and wave breaking statistics at a submesoscale front," J. Phys. Ocean. **52**, 289–304 (2022).
[26]See supplementary material at https://doi.org/10.1121/10.0021969 for aerial video of the ocean surface, synchronized with the acoustic surface projections.